Materials Advances

ROYAL SOCIETY OF CHEMISTRY

PAPER

View Article Online
View Journal | View Issue

Cite this: *Mater. Adv.*, 2024, 5, 652

First-principles modelling of the thermoelectric properties of n-type $CaTiO_3$, $SrTiO_3$ and $BaTiO_3$†

Alveena Z. Khan, Joseph M. Flitcroft and Jonathan M. Skelton *

Mitigating anthropogenic climate change requires a package of technologies including methods to improve the efficiency of energy-intensive transportation and industry. Thermoelectric (TE) power, which harnesses the Seebeck effect in a TE material to extract electrical energy from a temperature gradient, is a proven technology with the potential to meet this need. Oxide-based TEs are desirable for their low cost, high chemical stability and low toxicity, but are generally limited by a low electrical conductivity and high thermal conductivity. In this study, we employ a fully *ab initio* approach to predict the electrical and thermal transport and thermoelectric figure of merit ZT of the oxide perovskites $CaTiO_3$, $SrTiO_3$ and $BaTiO_3$ as a function of carrier concentration and temperature. We predict that carrier concentrations of $n \approx 10^{21}$ cm^{-3} are required to optimise the thermoelectric power factor, and that the piezoelectric scattering in rhombohedral $BaTiO_3$ limits the electrical conductivity compared to the other two systems. We find that the lattice thermal conductivity κ_{latt} is primarily determined by the structure type and chemical bonding through the phonon group velocities. We predict that $CaTiO_3$ and $SrTiO_3$ can achieve $ZT > 1$ at high temperature, and that the ZT of $SrTiO_3$ could be further enhanced by the impact of doping or alloying to obtain the required n on the κ_{latt}. The favourable comparison to experimental measurements suggests that this modelling approach has considerable predictive power, and could therefore serve as a valuable complement to experiments to identify new high-performance oxide TEs.

Received 30th August 2023,
Accepted 6th December 2023

DOI: 10.1039/d3ma00624g

rsc.li/materials-advances

1 Introduction

With continued growth in the global demand for energy and the urgent need to reduce greenhouse gas (GHG) emissions to limit anthropogenic climate change, the importance of technologies to provide clean energy and enhance the efficiency of energy use cannot be understated. A substantial proportion of the industry and technology that underpin modern life generates waste heat, with an estimated 60% of global energy lost through this route.[1] In particular, the difficult-to-decarbonise industry and transport sectors were estimated to be responsible for ~24 and 16% of GHG emissions in 2016,[2,3] highlighting the significant potential for reductions from improving efficiency.

Thermoelectric generators (TEGs) are solid-state devices that convert thermal energy directly to electricity *via* the Seebeck effect in a thermoelectric material. TEGs have no moving parts and are thus easy to maintain, have proven reliability in the aerospace industry, and are potentially scaleable to a wide range of applications.[3] The performance of a TE material is measured using the dimensionless figure of merit ZT defined by:[1,3]

$$ZT = \frac{S^2\sigma}{\kappa_{latt} + \kappa_{el}}T \quad (1)$$

where S is the Seebeck coefficient, σ is the electrical conductivity, $S^2\sigma$ is the thermoelectric power factor (PF), $\kappa = \kappa_{el} + \kappa_{latt}$ is the sum of the lattice (phonon) and electronic thermal conductivity, and T is the absolute temperature.

To optimise the ZT, the power factor should be maximised and the thermal conductivity minimised. S, σ, and κ_{el} depend on the electronic structure and are typically related through the carrier concentration n such that increasing n increases the σ and κ_{el} but reduces the S.[1] Materials-engineering strategies such as "band convergence" can in some case enhance the S without degrading the conductivity, but aside from these optimising the electrical properties entails balancing the σ, S and κ_{el} by optimising n, and the best balance is typically found in heavily-doped semiconductors. On the other hand, the lattice thermal conductivity is independent of the electrical properties and depends on the material structure and chemical bonding. The links between structure/composition and κ_{latt} are

Department of Chemistry, University of Manchester, Oxford Road, Manchester M13 9PL, UK. E-mail: jonathan.skelton@manchester.ac.uk

† Electronic supplementary information (ESI) available: Comparison of calculations on $SrTiO_3$ to measurements on doped single crystals, calculated electronic band structures and density of states curves, calculated electron scattering rates, and plots showing the anisotropy in the calculated electrical transport properties, lattice thermal conductivity and thermoelectric figure of merit. See DOI: https://doi.org/10.1039/d3ma00624g

at present not well understood, but low κ_{latt} is often associated with materials composed of heavy elements, with weak chemical bonding, and/or with strongly-anharmonic lattice dynamics arising from *e.g.* displacive phase transitions and active lone pairs.[4–8]

The current industry standard TEs are Bi_2Te_3 for applications around room temperature ($ZT \approx 1$ from 350–450 K)[3] and PbTe for high-temperature applications ($ZT = 2.2$ at 915 K),[9] due to their favourable electronic structure and intrinsically low thermal conductivity.[10,11] However, the low elemental abundance of Te and the environmental toxicity of Pb all but rule out widespread deployment, restricting Bi_2Te_3- and PbTe-based TEGs to niche applications.[12] Mass production of TEGs thus requires alternative candidate materials to be found that balance high performance against sustainability and cost requirements.

Oxide materials are attractive for their low toxicity, low cost, and high chemical robustness, which make them particularly suitable for high-temperature automotive and industrial applications. However, while oxides often show large Seebeck coefficients, they also tend to have low electrical conductivity, high lattice thermal conductivity, and hence low *ZT*. There has therefore been substantial research into enhancing the σ and minimising the κ_{latt} of oxides, for example by doping and alloying. Reports of large theromelectric power factors in cobaltites in the 1990s initiated research into several families of materials,[13] leading to promising candidates including the p-type layered cobaltites Na_xCoO_2,[13–16] $Ca_3Co_4O_9$[17–19] and $Bi_2Sr_2Co_2O_y$,[20–22] and n-type ZnO[23], $SrTiO_3$[24–26] and $CaMnO_3$.[27,28] Of these, $SrTiO_3$ is among the most promising and widely studied thermoelectric oxide perovskite due to its chemical flexibility and high thermal stability.[29] However, there have been relatively few studies of the thermoelectric properties of $CaTiO_3$ and $BaTiO_3$,[30–32] particularly in the non-cubic space groups adopted by these systems at low-to-mid temperature.

The major challenge to designing high-performance TEs is navigating the space of interlinked physical properties that need to be optimised. In this context, all four of the quantities in the *ZT* equation are amenable to first-principles calculations, allowing, in principle, the *ZT* to be estimated as a function of the extrinsic carrier concentration (''doping level'') and temperature through a fully *ab initio* approach. In particular, a recent approach to calculating electronic transport properties, including a model for the electron relaxation times,[33] when paired with established approaches to predicting the κ_{latt},[34] has been shown to yield very good predictions for the well-characterised tin chalcogenides SnS and SnSe[35] and has been applied to novel candidate TEs including the ternary oxide $Bi_2Sn_2O_7$[36] and the quaternary oxysulphide $Y_2Ti_2O_5S_2$.[37] This type of calculation can provide valuable guidance to experiments as to the conditions where the maximum *ZT* is likely to be obtained and thus define potential application areas for a material.

In this work, we apply this approach to the Group II titanate perovskites $CaTiO_3$ (CTO), $SrTiO_3$ (STO) and $BaTiO_3$ (BTO), in the orthorhombic *Pnma*, tetragonal *I*4/*mcm* and rhombohedral *R*3*m* phases, respectively, allowing us to investigate the impact of the A-site cation and structure type on the thermoelectric performance. We find that STO has the best electrical transport properties, whereas the lower-symmetry structure of CTO lends itself to a low κ_{latt}. On the other hand, BTO is predicted to have a relatively high κ_{latt} and limited σ due to piezoelectric scattering leading to short electron lifetimes. We predict maximal $ZT_{max} \approx 0.2$ and 0.5 at mid and high temperatures of 600 and 1000 K and doping levels on the order of 10^{21} cm^{-3}. Industrially viable $ZT_{max} > 1$ are only obtained at temperatures above $\sim$1500 K. The low-temperature *ZT* is limited by the large κ_{latt}, arising from the strong chemical bonding and resultant large phonon group velocities, and could be mitigated as a positive side effect of the chemical modifications required to optimise the electrical properties. Our findings provide valuable insight to ongoing efforts to optimise these systems, and, importantly, demonstrate that this *ab initio* workflow can provide useful predictions to support ongoing efforts to obtain high-performance oxide TEs.

2 Methodology

Calculations were performed using pseudopotential plane wave density functional theory (DFT) as implemented in the Vienna *Ab initio* Simulation Package (VASP) code.[42]

Initial structures of $CaTiO_3$, $SrTiO_3$ and $BaTiO_3$ in the *Pnma*, *I*4/*mcm* and *R*3*m* spacegroups, respectively, were taken from the Materials Project (MP) database[43] (**mp-4019**, **mp-4651**, **mp-5020**) and optimised to tight tolerances of 10^{-8} eV on the total energy and 10^{-3} eV Å^{-1} on the forces.

Electron exchange and correlation were described using the PBEsol generalised-gradient approximation (GGA) functional.[44] The ion cores were modelled using projector-augmented wave (PAW) pseudopotentials[45,46] with valence configurations of: Ti – $3d^2\ 4s^2$; O – $2s^2\ 2p^4$; Ca – $3p^6\ 4s^2$; Sr – $4s^2\ 4p^6\ 5s^2$; and Ba – $5s^2\ 5p^6\ 6s^2$. The valence wavefunctions were described using a plane-wave basis with an 800 eV kinetic-energy cutoff, and the electronic Brillouin zones were sampled using Γ-centred Monkhorst–Pack $\boldsymbol{k}$-point meshes[47] with $4 \times 4 \times 2$, $5 \times 5 \times 3$ and $4 \times 4 \times 4$ subdivisions for the CTO, STO and BTO primitive cells, respectively. These parameters were chosen based on explicit testing to converge the absolute total energies to <1 meV atom^{-1} and the external pressure to <1 kbar (0.1 GPa).

Lattice-dynamics and thermal-conductivity calculations were performed using the supercell finite-differences approach implemented in the Phonopy and Phono3py packages.[34,48]

The second-order (harmonic) force constants were computed in a $4 \times 2 \times 4$ expansion of the CTO unit cell (640 atoms), and $4 \times 4 \times 4$ expansions of the STO and BTO primitive unit cells (640/320 atoms). Atom-projected phonon density of states (PDoS) curves were computed by interpolating the phonon frequencies onto regular Γ-centred $\boldsymbol{q}$-point grids with $12 \times 12 \times 12$ subdivisions using the linear tetrahedron method for Brillouin-zone integration. Phonon dispersions were obtained by evaluating the frequencies at strings of $\boldsymbol{q}$-points passing through the high-symmetry points in the respective Brillouin zones. Non-analytical corrections to the dynamical matrices at $\boldsymbol{q} \rightarrow \Gamma$ were included

using the approach in ref. 49 using Born effective-charge tensors $\boldsymbol{Z}^*$ and high-frequency dielectric constants $\boldsymbol{\varepsilon}_\infty$ computed using the density-functional perturbation theory (DFPT) routines in VASP.[50]

The third-order (anharmonic) force constants were computed in a $2 \times 1 \times 2$ expansion of the CTO unit cell (80 atoms) and $2 \times 2 \times 2$ expansions of the STO and BTO primitive cells (80/135 atoms). The lattice thermal conductivities were then calculated within the single-mode relaxation-time approximation (SM-RTA) by combining the second- and third-order force constants to obtain modal heat capacities C_λ, group velocities $\boldsymbol{\nu}_\lambda$ and lifetimes τ_λ on uniform Γ-centered $8 \times 8 \times 8$ $\boldsymbol{q}$-point sampling meshes. This mesh was chosen based on explicit testing to converge the average of the three diagonal components of the $\boldsymbol{\kappa}_{\text{latt}}$ tensors, $\kappa_{\text{ave}} = (\kappa_{xx} + \kappa_{yy} + \kappa_{zz})/3$, to within 5% of the values obtained with larger sampling meshes.

Electronic transport calculations were performed using the AMSET code.[33]

Accurate band gaps E_g were obtained using non self-consistent calculations with the HSE06 hybrid functional,[51,52] where a single-point calculation with PBE[53] is performed to obtain a set of Kohn–Sham orbitals and the band energies recalculated with HSE06 using the PBE orbitals. Uniform band-structure calculations were then performed with PBEsol and denser $8 \times 8 \times 4$, $10 \times 10 \times 6$ and $8 \times 8 \times 8$ $\boldsymbol{k}$-point meshes for CTO, STO and BTO, respectively, and the bandgaps increased to the HSE06 values using scissors operators. These meshes were further interpolated to a $\sim 30\times$ higher density when calculating the transport properties.

AMSET estimates the electronic relaxation times by summing scattering rates from four different processes, *viz.* acoustic deformation potential (ADP), polar optic phonon (POP), piezoelectric (PIE), and ionised impurity (IMP) scattering, requiring a range of material properties to be calculated. Deformation potentials were computed by performing a series of single-point energy calculations on deformed structures, generated using AMSET, with PBEsol. High-frequency dielectric constants $\boldsymbol{\varepsilon}_\infty$, Born effective charges $\boldsymbol{Z}^*$ and piezoelectric moduli were determined using DFPT.[50] For these calculations, convergence tests indicated that $3\times$ denser $\boldsymbol{k}$-point sampling along each reciprocal-lattice vector compared to the "base" meshes used for geometry optimisation were required to converge the $\boldsymbol{\varepsilon}_\infty$. The $\boldsymbol{Z}^*$ were used to determine the infrared (IR) activities of the phonon modes at $\boldsymbol{q} = \Gamma$,[54,55] evaluated with Phonopy, and to calculate the polar optic phonon (POP) frequencies. The elastic constants C_{ij} and ionic contributions to the dielectric constant, $\boldsymbol{\varepsilon}_{\text{ionic}}$, were computed using PBEsol and the finite-differences routines in VASP, the latter of which was used to obtain the static dielectric constant $\boldsymbol{\varepsilon}_s = \boldsymbol{\varepsilon}_\infty + \boldsymbol{\varepsilon}_{\text{ionic}}$.

3 Results and discussion

3.1 Optimised structures

The optimised structures of CTO, STO and BTO, converted to the conventional crystallographic unit cells, are shown in Fig. 1. The ABX_3 structure comprises a network of corner-sharing BX_6 octahedra surrounding cuboctahedral cavities filled by the A-site cations. The ideal perovskite structure is cubic with the *Pm3m* spacegroup, but this is often not the lowest-energy configuration. Instead, many perovskites adopt one of a rich variety of structures obtained by rigid tilting of the octahedra and/or by displacements of the A- or B-site cations from their ideal positions in the cubic phase.[56,57] In this case, the higher-symmetry rhombohedral *R3m* structure of BTO is derived from the cubic aristotype by a displacement of the B-site cation along the [111] direction,[57] while the lower-symmetry tetragonal *I4/mcm* structure of STO is derived by a single octahedral tilt and the orthorhombic *Pnma* structure of CTO is derived by three independent tilts.[56]

The optimised lattice parameters are collected in Table 1 and compared to experimental measurements from the literature. The lattice parameters of CTO, STO and BTO are within 2%, 1% and 0.5%, respectively, of the experimental measurements. We note that our "athermal" optimised structures are those at 0 K without corrections for the vibrational zero-point energy, whereas the experimental measurements are performed at finite temperature and may include changes to the lattice

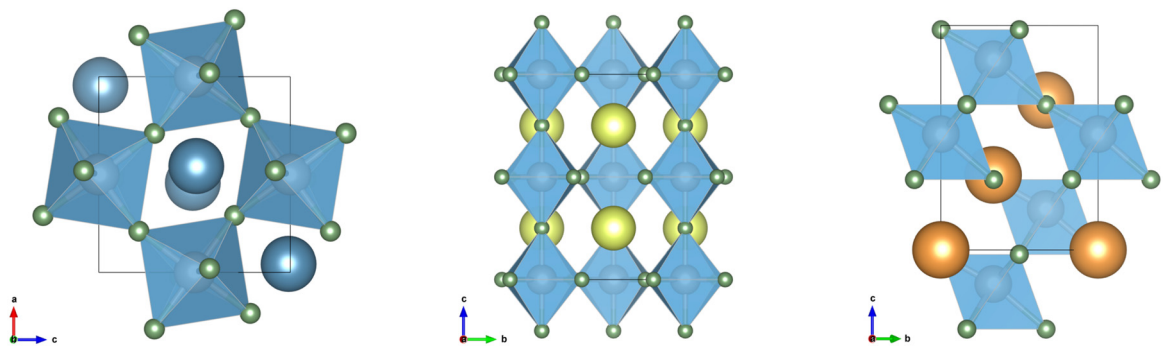

a) $CaTiO_3$ (*Pnma*) b) $SrTiO_3$ (*I4/mcm*) c) $BaTiO_3$ (*R3m*)

Fig. 1 Conventional cells of $CaTiO_3$ in the *Pnma* space group (a), $SrTiO_3$ in the *I4/mcm* space group (b) and $BaTiO_3$ in the *R3m* space group (c). Atom colours: Ca – blue; Sr – yellow; Ba – orange; Ti – grey; O – green. These images were prepared using the VESTA software.[38]

Table 1 Optimised lattice parameters of the conventional cells of *Pnma* $CaTiO_3$, *I*4/*mcm* $SrTiO_3$, and *R*3*m* $BaTiO_3$ compared to experimental values from the literature. The percentage differences between the calculated and measured values are given in parentheses

		a (Å)	b (Å)	c (Å)	V (Å^3)
$CaTiO_3$	Expt[39]	5.379	7.639	5.436	223
	Opt	5.464 (1.58)	7.615 (−0.31)	5.353 (−1.53)	223 (0)
$SrTiO_3$	Expt[40]	5.514	—	7.807	237
	Opt	5.505 (−0.16)	—	7.850 (0.55)	238 (0.42)
$BaTiO_3$	Expt[41]	5.651	—	6.948	192
	Opt	5.661 (0.18)	—	6.950 (0.03)	193 (0.39)

constants due to thermal expansion or contraction, so we therefore consider these small differences acceptable. Our optimised lattice parameters are also within 5% of those of the initial MP structures, although these are optimised with the PBE functional, which typically overestimates lattice parameters and unit-cell volumes relative to experiments.

3.2 Lattice dynamics and lattice thermal conductivity

The calculated phonon dispersion and density of states (DoS) curves for CTO, STO and BTO are shown in Fig. 2.

BTO has $n_a = 5$ atoms in the primitive cell, resulting in $3n_a = 15$ branches at each phonon wavevector $\boldsymbol{q}$. CTO and STO have $n_a = 10$ and 20, respectively, and thus considerably more complex phonon spectra with 30 and 60 bands at each $\boldsymbol{q}$. This increase in complexity due to the larger primitive unit cells is compounded by the reduction in symmetry resulting in fewer degenerate bands. The absence of imaginary harmonic modes in all three phonon dispersion curves indicates that the three structures are dynamically stable.

In all three systems the A-site cations make the largest contributions to the low-frequency acoustic modes. Heavier cations produce lower-frequency, sharper peaks in the PDoS consistent with ''rattling'' behaviour, indicating weaker interactions between the A-site cations and the TiO_6 octahedral framework. The higher-frequency optic modes are predominantly due to the motion of the Ti and O atoms and correspond to deformations of the TiO_6 octahedra. In all three systems the optic modes are separated into a broad band of mid-frequency modes involving motion of the Ti and O atoms and an isolated group of high-frequency modes associated primarily with O. The calculated phonon spectra of STO and CTO agree well with previous calculations.[59,60] While we were not able to find reference phonon spectra for *R*3*m* BTO to compare to, the good agreement for STO and CTO gives us confidence in our calculation on BTO.

To predict the lattice thermal conductivity $\boldsymbol{\kappa}_{latt}$, we used the single-mode relaxation time approximation (SM-RTA) model.[34] The $\boldsymbol{\kappa}_{latt}$ are 3 × 3 tensors, where the diagonal elements correspond to transport along the three Cartesian directions. Since practical thermoelectric devices tend to be based around thin films or pressed pellets composed of randomly-oriented crystal grains, we focus mainly on the scalar average $\kappa_{ave} = (\kappa_{xx} + \kappa_{yy} + \kappa_{zz})/3$, which we also denote κ_{latt}. Fig. 3(a) shows the predicted κ_{latt} of the three perovskites as a function of temperature, and values at $T = 1000$ K are collected in Table 2.

The predicted averaged thermal conductivities fall in the order of CTO < STO ≈ BTO. The κ_{latt} of CTO, STO and BTO are 3.2, 4.4 and 4.5 W m^{-1} K^{-1} at 300 K, and decrease sharply with temperature to 0.96, 1.4 and 1.3 W m^{-1} K^{-1} at 1000 K.

Ref. 61 reports total thermal conductivities of 4 and 3 W m^{-1} K^{-1} for STO at 300 and 1000 K, respectively, while ref. 62 reports a larger 6.5 W m^{-1} K^{-1} at 400 K and a comparable $\kappa = 3.25$ W m^{-1} K^{-1} at 1000 K. The measurements in ref. 63 on La- and Nb-doped single crystals cite even higher κ_{latt} of ∼8–10 W m^{-1} K^{-1} at 300 K, but similar values around 3 W m^{-1} K^{-1} at 1000 K. The factor of three variation in the low-temperature κ_{latt} highlights the sensitivity of these measurements to the sample preparation and morphology. In principle, the single-crystal measurements should be most comparable to our calculations, but we find we consistently underestimate the experiments by a factor of ∼2× (see Section 1 of the ESI†). Given that the tetragonal-to-cubic phase transition in STO occurs around 100 K,[64] we would expect the crystals to be in the higher-symmetry cubic phase, so we tentatively put this discrepancy down to us modelling the tetragonal structure.

On the other hand, comparison to the measurements on $CaTiO_3$ in ref. 30, which obtained κ_{latt} ≈ 2–4.5 and 2–3 W m^{-1} K^{-1} at 300 and 1000 K, suggest that our calculations on this system also underestimate the κ_{latt} at high temperature. Given that the orthorhombic-to-cubic transition in CTO occurs well above 1000 K,[65] the experiments and calculations for this system should be on the same crystal phase.

Both our predictions and the experimental measurements are nevertheless considerably larger than the κ_{latt} of flagship materials such as Bi_2Te_3 and SnSe, for which we calculated lattice thermal conductivities of 0.88 and 1.58 W m^{-1} K^{-1} in previous studies using similar methodology (the experimental values are 1.28/1.37[66,67] and 0.5–1.4 W m^{-1} K^{-1}).[68] However, the measurements in ref. 30, and experiments on high-entropy perovskite oxides,[69] demonstrate that the κ_{latt} can be significantly reduced by controlling the chemical composition, providing a means to mitigate this.

Given that the anisotropy in the thermal transport of the flagship thermoelectric SnSe plays an important role in its large high-temperature figure of merit,[5,70] we also investigated the anisotropy in the κ_{latt} of CTO, STO and BTO (Table 2 and Fig. S4–S6, ESI†). For the tetragonal *I*4/*mcm* and rhombohedral *R*3*m* spacegroups of STO and BTO, respectively, symmetry dictates that $\kappa_{xx} = \kappa_{yy} \neq \kappa_{zz}$, whereas in the lower-symmetry orthorhombic *Pnma* spacegroup of CTO $\kappa_{xx} \neq \kappa_{yy} \neq \kappa_{zz}$. For STO and BTO, we predict $\kappa_{xx} = \kappa_{yy} < \kappa_{zz}$, while for CTO we predict $\kappa_{xx} \approx \kappa_{yy} > \kappa_{zz}$. The anisotropy in CTO and BTO is relatively small, with a maximum variation of 4–5% in the directional components relative to the average, whereas STO shows a larger variation of around 15%.

Low κ_{latt} is often associated with materials composed of heavy elements with weak chemical bonds,[4] and it is therefore interesting that, given CTO is the lightest of the three materials (*cf.* Table 2), it also has the lowest κ_{latt}. This indicates that

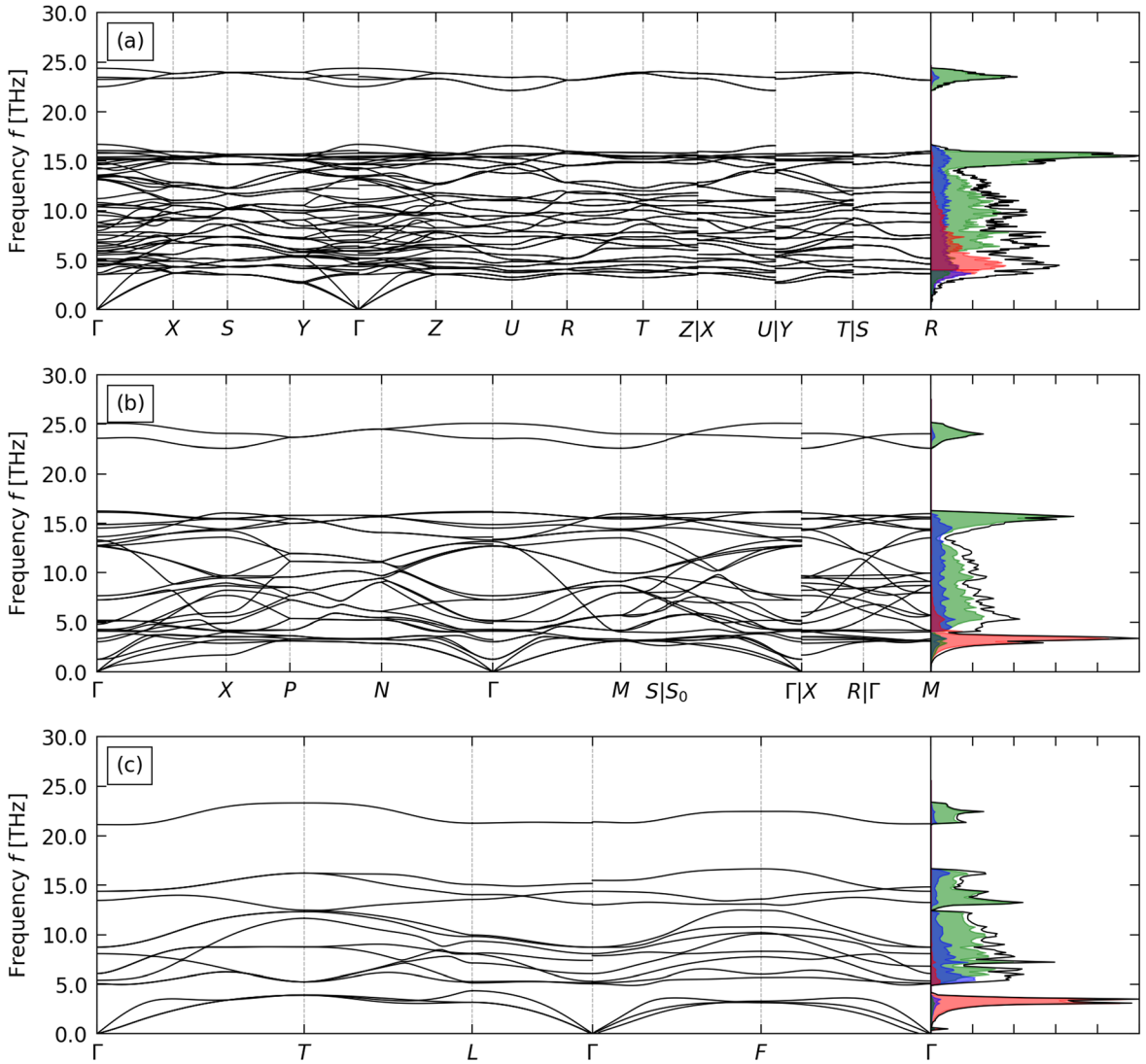

Fig. 2 Calculated phonon dispersion and density of states (DoS) curves of $CaTiO_3$ (a), $SrTiO_3$ (b), and $BaTiO_3$ (c). On each DoS plot, the total DoS is shown in black, and projections onto the A-site cation, Ti and O atoms are shown in red, blue, and green respectively.

differences in structure and bonding, rather than the mass of the A-site cation, play a significant role in determining the lattice thermal conductivity. To investigate this further, we applied the constant relaxation-time approximation (CRTA)

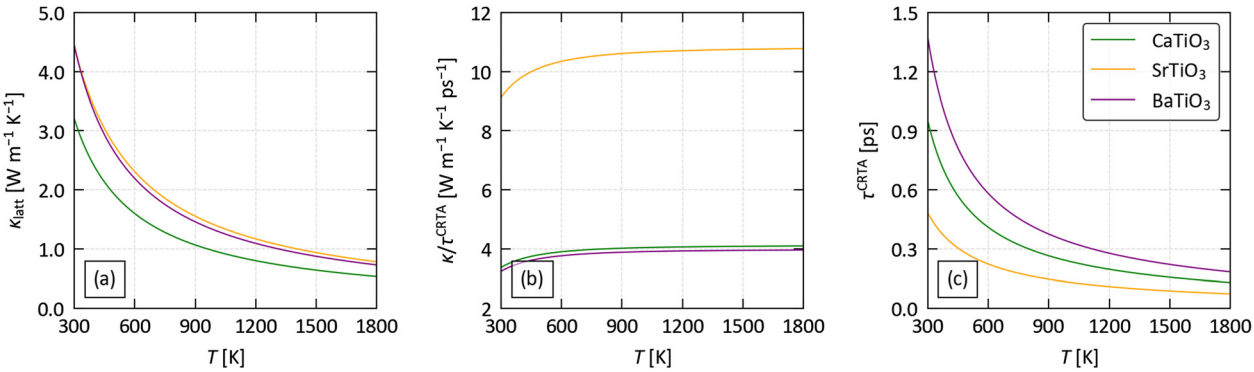

Fig. 3 Analysis of the predicted lattice thermal conductivity of $CaTiO_3$, $SrTiO_3$ and $BaTiO_3$ using the constant relaxation-time approximation defined in eqn (2): averaged thermal conductivity κ_{latt} (a), harmonic term κ/τ^{CTRA} (b) and averaged lifetime τ^{CTRA} (c) as a function of temperature.

Table 2 Calculated lattice thermal conductivity of the three perovskite structures examined in this work at T = 1000 K. Each row gives the three diagonal components of the $\boldsymbol{\kappa}_{\text{latt}}$ tensors, κ_{xx}, κ_{yy} and κ_{zz}, together with the diagonal average κ_{ave} and its decomposition into harmonic and lifetimes components $(\boldsymbol{\kappa}/\tau^{\text{CRTA}})_{\text{ave}}$ and τ^{CRTA} as defined in eqn (2). The atomic masses and radii[58] of the A-site cations are also listed for comparison

	m_A [amu]	r_A [pm]	$\boldsymbol{\kappa}_{\text{latt}}$ [W m^{-1} K^{-1}] κ_{xx}	κ_{yy}	κ_{zz}	κ_{ave}	$(\boldsymbol{\kappa}/\tau^{\text{CRTA}})_{\text{ave}}$ [W m^{-1} K^{-1} p^{-1}]	τ^{CRTA} [ps]
$CaTiO_3$	40.1	180	0.984	0.980	0.916	0.960	4.04	0.237
$SrTiO_3$	87.6	200	1.293	—	1.614	1.400	10.65	0.131
$BaTiO_3$	137	215	1.286	—	1.366	1.313	3.91	0.336

analysis developed in previous work[71,72] to the κ_{ave}. In this model, the $\boldsymbol{\kappa}_{\text{latt}}$ is written as:

$$\begin{aligned}\boldsymbol{\kappa}_{\text{latt}}(T) &= \tau^{\text{CRTA}}(T) \times \frac{1}{N_{\boldsymbol{q}} V} \sum_{\lambda} \frac{\boldsymbol{\kappa}_{\lambda}(T)}{\tau_{\lambda}(T)} \\ &= \tau^{\text{CRTA}}(T) \times \frac{1}{N_{\boldsymbol{q}} V} \sum_{\lambda} C_{\lambda}(T) \boldsymbol{v}_{\lambda} \otimes \boldsymbol{v}_{\lambda}\end{aligned} \tag{2}$$

where $\boldsymbol{\kappa}_{\lambda}$ are the microscopic contributions to the $\boldsymbol{\kappa}_{\text{latt}}$ from individual phonon modes λ with heat capacities C_{λ}, group velocities $\boldsymbol{\nu}_{\lambda}$ and lifetimes τ_{λ}, and the sum is normalised by the cell volume V and the number of phonon wavevectors $N_{\boldsymbol{q}}$ included in the summation. (The analysis was applied to the scalar κ_{ave} by taking the average of $(\boldsymbol{\kappa}/\tau^{\text{CRTA}})$ and choosing the τ^{CRTA} to be consistent with the κ_{ave}.)

The averaged $(\kappa/\tau^{\text{CRTA}})$ and τ^{CRTA} of the three systems are shown in Fig. 3(b) and (c), and the values at 1000 K are included in Table 2.

In our previous work on Si clathrates we found a strong correlation between the group velocities and the number of atoms n_a in the primitive cell, and a secondary correlation with crystal symmetry (spacegroup).[73] Based on this, we would expect the $\kappa/\tau^{\text{CRTA}}$ to vary in the order BTO (rhombohedral, n_a = 5) > STO (tetragonal, n_a = 10) > CTO (orthorhombic, n_a = 20). CTO and STO follow this trend, with $\kappa/\tau^{\text{CRTA}}$ = 4 and 10.7 at 1000 K, whereas for BTO $\kappa/\tau^{\text{CRTA}}$ = 3.9 which is comparable to but slightly lower than CTO. This is consistent with the phonon dispersions in Fig. 2, which show a notably shallower dispersion for BTO, particularly in the low-frequency acoustic modes. The much larger $\kappa/\tau^{\text{CRTA}}$ of STO compared to CTO, despite the larger mass m_A of the A-site cation, suggests that this cannot be attributed to Ba having the largest m_A. One explanation is that accommodating the larger Ba cation places a strain on the TiO_6 octahedral framework, which may be reflected in the larger volume per formula unit of BTO compared to the similar volumes of CTO and STO (*cf.* Table 1). Another is that the off-centering of the B-site Ti^{4+} cation in the *R*3*m* structure has a larger impact on the chemical bonding in the TiO_6 octahedral framework than the rigid tilting in the *I*4/*mcm* and *Pnma* structures.

All three compounds show sub-picosecond averaged lifetimes τ^{CRTA} at 1000 K. The τ^{CRTA} vary by ~2.6× and show the opposite trend to the harmonic terms, *i.e.* are shortest for STO and longest for BTO. The combination of the 2.7× larger $\kappa/\tau^{\text{CRTA}}$ and shorter averaged lifetimes of STO compared to BTO result in the two systems having similar κ_{latt}, while the low group velocities and intermediate τ^{CRTA} of CTO lead to the lowest κ_{latt} of the three systems. The long τ^{CRTA} of BTO are perhaps also unexpected given the localised A-site feature in the phonon DoS (*cf.* Fig. 2). However, following a similar thought process to the analysis of the $\kappa/\tau^{\text{CRTA}}$, the larger radius r_A of the Ba cation (*cf.* Table 2) may limit its ability to rattle and produce the expected phonon scattering.

Compared to the flagship thermoelectrics SnSe and Bi_2Te_3, the $\kappa/\tau^{\text{CRTA}}$ at 300 K are much larger (3.24–9.12 W m^{-1} K^{-1} ps^{-1} compared to 0.37 and 0.2 W m^{-1} K^{-1} ps^{-1} for SnSe[72] and Bi_2Te_3[74]), whereas the τ^{CRTA} are shorter (0.48–1.37 ps compared to 4.23/4.41 ps for SnSe/Bi_2Te_3[72,74]). This is consistent with the stronger bonding in oxides, which would both produce larger group velocities but also stronger phonon interactions, and suggests that the common strategies for optimising the electrical properties (*e.g.* introducing oxygen vacancies and heavy doping[72]) would likely have a synergistic effect of reducing the lattice thermal conductivity. We defer further exploration of this to a future study.

3.3 Electronic structure and transport properties

The calculated electronic band structures of the three perovskites are provided in Fig. S7–S9 (ESI†), and the calculated electronic band gaps E_g are compared to previous experimental and theoretical studies in Table 3. The calculated E_g = 4.5 eV for CTO agrees well with the upper range of the experimental values reported in ref. 75. We were not able to find an experimental bandgap for *R*3*m* BTO, but our predicted E_g = 4.42 eV is consistent with the values of 4.9 and 5.18 eV obtained in previous theoretical studies.[76,77] (We attribute our smaller predicted value to our use of the screened HSE06 hybrid functional rather than the unscreened PBE0[78] used in ref. 76 and 77.) On the other hand, our predicted E_g = 4.15 eV for STO is considerably larger than the 3.4 eV predicted in previous calculations[79] and is also larger than the measured E_g = 3.25 eV of cubic STO.[80] Despite these discrepancies, all three perovskites are predicted to be insulators, and we would not expect the possible overestimation of the bandgap of STO to significantly impact the calculated electrical properties.

Table 3 Calculated electronic band gaps E_g of the three systems examined in this work compared to other experimental and theoretical studies where available

		E_g [eV]
$CaTiO_3$	Calcd (this work)	4.50 (direct)
	Expt[75]	4.38 (direct)
		3.80 (indirect)
		4.11
$SrTiO_3$	Calcd (this work)	4.15 (indirect)
	Expt[80]	3.25
$BaTiO_3$	Calcd (this work)	4.42 (indirect)
	Calcd[76]	5.18 (indirect)
	Calcd[77]	4.90

We therefore proceeded to use the semi-classical Boltzmann transport theory and approximate electron scattering models implemented in the AMSET code[33] to estimate the three electrical transport properties in eqn (1), *viz.* the Seebeck coefficient $\boldsymbol{S}$, electrical conductivity $\boldsymbol{\sigma}$ and electronic thermal conductivity $\boldsymbol{\kappa}_{\mathrm{el}}$.

In these calculations, the properties are determined for a series of extrinsic carrier concentrations ("doping levels") n and temperatures. The doping level is set by adjusting the Fermi level E_{F} in the electronic-structure calculation, and do not take into account the practicalities or potential impacts[81] of doping to obtain a given n. The electron relaxation times are

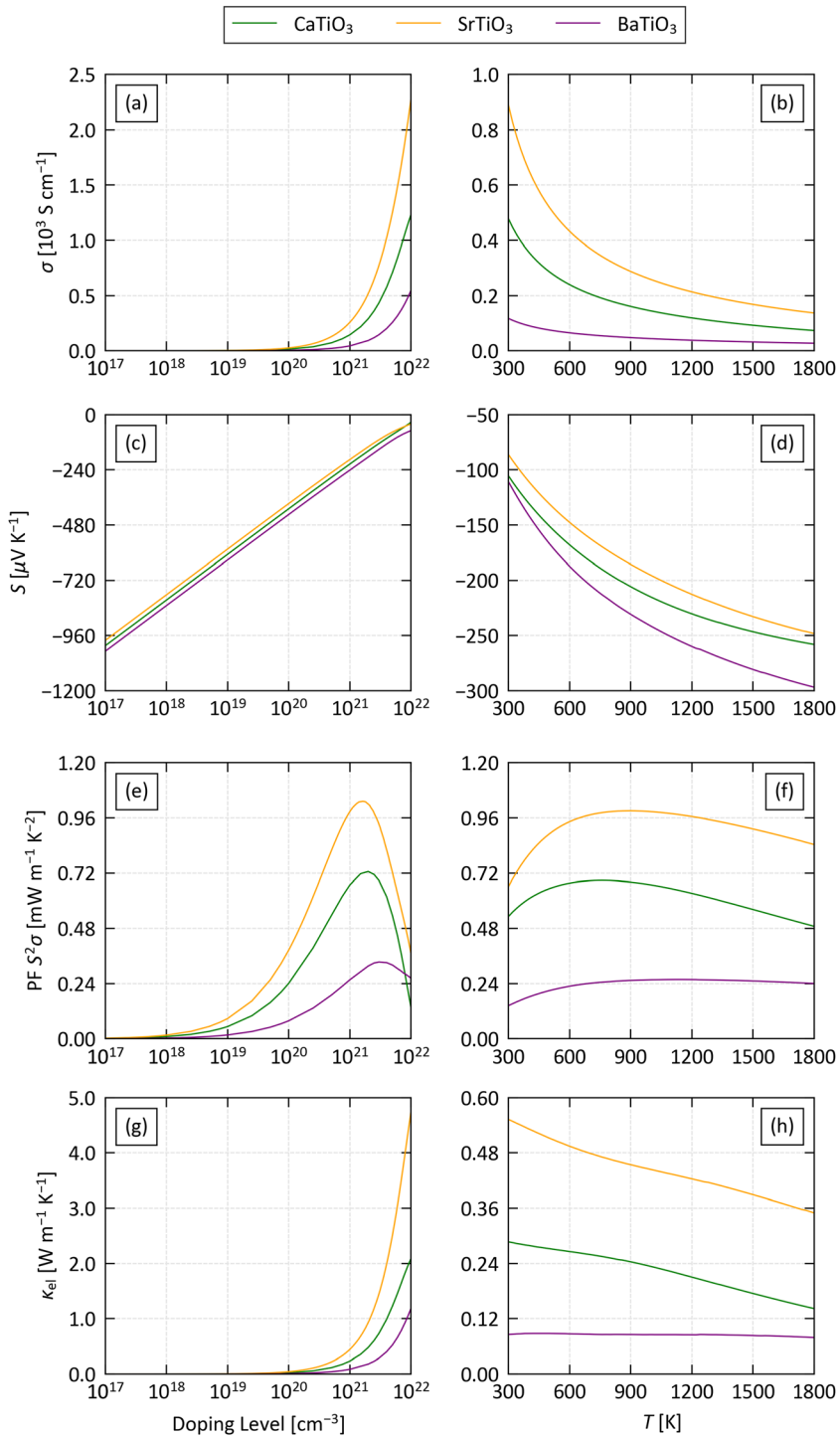

Fig. 4 Comparison of the calculated averaged electrical conductivity σ (a)/(b), Seebeck coefficient S (c)/(d) power factor $S^2\sigma$ (PF) (e)/(f) and electronic thermal conductivity κ_{el} (g)/(h) of the three structures examined in this work as a function of doping level at a fixed T = 1000 K (a)/(c)/(e)/(g) and as a function of temperature at a fixed doping level $n = 10^{21}$ cm^{-3} (b)/(d)/(f)/(h).

determined approximately by summing the rates from four scattering mechanisms, *viz.* acoustic deformation potential (ADP), piezoelectric (PIE), polar optical phonon (POP) and ionised impurity (IMP) scattering. Full details of these calculations are provided in ref. 33.

As for the $\boldsymbol{\kappa}_{\mathrm{latt}}$, the $\boldsymbol{\sigma}$, $\boldsymbol{S}$ and $\boldsymbol{\kappa}_{\mathrm{el}}$ are 3×3 tensors, and we again focus mainly on the scalar averages $(xx + yy + zz)/3$, which we denote σ, S and κ_{el} to distinguish them from the tensor quantities.

Fig. 4 shows the calculated electrical properties as a function of electron carrier concentration n between 10^{16} and 10^{22} cm^{-3} at a fixed $T = 1000$ K, and as a function of temperature between 300–1800 K at a fixed $n = 10^{21}$ cm^{-3}. Pristine STO has a relatively low n on the order of 10^{15} cm^{-3}, as expected for an insulator.[82] However, depending on the preparation conditions, experimental samples can have a high concentration of oxygen vacancies that act as electron donors and produce a much higher n, and carrier concentrations as high as 3.5×10^{20} cm^{-3} have been reported in undoped $SrTiO_3$ thin films.[83] The chemical flexibility of the perovskite structure also allows it to accommodate a wide range of dopants that can enhance the n, yielding concentrations well in excess of 10^{21} cm^{-3} in experiments.[82–85] The fixed $n = 10^{21}$ cm^{-3} is therefore a conservative estimate of what should be possible in experiments. While perovskites are stable to high temperatures, we took $T = 1000$ K as a reference point to match the high-temperature heat-recovery scenario outlined in ref. 86.

At $T = 1000$ K and the lowest $n = 10^{16}$ cm^{-3} we studied, the S are on the order of -1200 μV K^{-1} and decrease monotonically with n to around -50 μV K^{-1} at $n = 10^{22}$ cm^{-3}. On the other hand, the σ are negligible up to $n \approx 10^{19}$ cm^{-3} and increase sharply at higher carrier concentrations. The increase in the conductivity dominates the PF $S^2\sigma$ up to $n \simeq 10^{21} - 5 \times 10^{22}$ cm^{-3} cm^{-3}, while at larger n the decrease in S becomes dominant, producing a maximum in the PF around 10^{21} cm^{-3}. We therefore conclude that carrier concentrations above $\sim 10^{19}$ cm^{-3} are necessary to obtain a reasonable PF, but very high n are detrimental. On the other hand, the κ_{el} increases with σ following the Wiedemann–Franz law:

$$\kappa_{\mathrm{el}}(T) = L\sigma(T)T \tag{3}$$

where L is the Lorentz number. At the n where the PFs are maximised, the κ_{el} are <1 W m^{-1} K^{-1}, whereas at the largest $n = 10^{22}$ cm^{-3} we modelled they reach comparatively large values of 1–5 W m^{-1} K^{-1}. Given that the κ_{el} appears in the denominator of eqn (1), this would combine with the reduced S and PF to limit the TE performance.

At a fixed $n = 10^{21}$ cm^{-3} the σ decrease with temperature in all three systems, indicative of degenerate semiconductors with metallic-like conductivity. On the other hand, the absolute values of the S increase with temperature from 100 μV K^{-1} at 200 K to around 200–250 μV K^{-1} at 1200 K. This balance results in a rise in the PF from 300 K and a subsequent levelling off from $\sim$750 K. The temperature dependence of the κ_{el} mirrors the behaviour of the electrical conductivity, in keeping with the Wiedemann–Franz law, but at this modest n the values are a relatively small 0.1–0.6 W m^{-1} K^{-1}.

The three systems are predicted to have very similar Seebeck coefficients, but the conductivities, power factors and electrical thermal conductivities fall in the order of STO > CTO > BTO. Our calculations predict a maximum PF around 1 mW m^{-1} K^{-1} for STO at $n = 2 \times 10^{21}$ cm^{-3} and $T = 1360$ K, and under these conditions the κ_{el} is on the order of 0.8 W m^{-1} K^{-1}. Conversely, the low σ of BTO results in a maximum PF of 0.4 mW m^{-1} K^{-1} at $n = 5 \times 10^{21}$ cm^{-3} and $T = 1640$ K. Comparing the scattering rates of the three materials at $n = 10^{21}$ cm^{-3} and $T = 1000$ K (Fig. S10–S12, ESI†) indicates that the low σ of BTO is due to the impact of piezoelectric (PIE) scattering on the electron relaxation times – this mechanism is only active in the non-centrosymmetric *R3m* spacegroup, and indicates that the B-site cation off-centering may be detrimental to the electrical transport.

Finally, a comparison of the *xx*, *yy* anad *zz* components of the electrical transport tensors to the average values discussed here shows relatively minimal anisotropy (Fig. S13–S15, ESI†). The Seebeck coefficients of all three systems are essentially isotropic. The conductivity in STO and BTO is also largely isotropic, resulting in minimal variability in the PFs and κ_{el}. On the other hand, the σ of CTO shows modest anisotropy such that the *a* and *b* directions represent "easy" and "hard" axes for transport, respectively, and the PFs are $\sim$0.1 mW m^{-1} K^{-2} (15%) larger/smaller than the average.

We previously employed this procedure to calculate the electrical properties of SnS and SnSe and obtained very good agreement with experimental measurements.[35]

Measurements on 20% La-doped cubic STO obtained a σ, S and PF on the order of 150 S cm^{-1}, -250 μV K^{-1} and 0.9 mW m^{-1} K^{-2} at 1000 K.[61] With a comparable $n = 3 \times 10^{21}$ cm^{-3} we predict a larger $\sigma = 775$ S cm^{-1}, a smaller absolute $S = -109$ μV K^{-1}, and a similar PF of 0.93 mW m^{-1} K^{-2}. Measurements on $(La_{0.12}Sr_{0.88})_{0.95}TiO_3$ yielded $\sigma \approx 100$ S cm^{-1}, $S \approx -200$ μV K^{-1} and $S^2\sigma \approx 0.3$–0.4 mW m^{-1} K^{-2} at 900 K,[62] and using a (estimated) comparable $n = 2.5 \times 10^{20}$ cm^{-3} we predict values of $\sigma = 71$ S cm^{-1}, $S = -299$ μV K^{-1} and $S^2\sigma = 0.63$ mW m^{-1} K^{-2}. Finally, measurements on Nb-doped $SrTiO_3$ films, with $n \approx 1.5$–2×10^{21} in the thickest samples, obtained a maximum σ and S around 600 S cm^{-1} and -120 μV K^{-1} at room temperature,[87] and we predict $\sigma = 238$ S cm^{-1} and $S = -44$ μV K^{-1} with $n = 2.5 \times 10^{21}$ cm^{-3}.

We also performed a more quantitative comparison of our predicted σ and S to measurements on the four doped single-crystal STO samples reported in ref. 63 (Section 1 of the ESI†). This shows that the calculations tend to over- and underestimate the carrier concentration required to achieve a given σ at low and high T, respectively. On the other hand, the calculations appear to consistently underestimate the n required to obtain a given S. Equivalently, for a given n the comparison suggests the calculations are likely to under- or overestimate the σ compared to experiments at low and high temperature, and, given the monotonic reduction in the absolute value of S with carrier concentration, to underestimate the S.

The vacancy/dopant concentrations in these studies are up to several tens of at%, which means that the assumption of the rigid-band approximation, *i.e.* that the defects do not change the host electronic structure beyond simply increasing the n, may not be valid.[81] Also, the grain boundaries in "granular" bulk materials composed of randomly-oriented crystal grains, such as pressed pellets or consolidated powders, can result in energy filtering and carrier trapping, which can impact upon the S and σ.[88] This may be applicable to some of the experimental samples, and similar phenomena could arise from the point defects in the heavily-doped single-crystal STO samples in ref. 63. Finally, as for the κ_{latt}, some of the discrepancies could also be due to the measurements being carried out on the cubic rather than the tetragonal phase.

STO is the most widely-studied of the three perovskites, but we were able to find measurements on a variety of $(Ca_{1-x}La_x)TiO_{3-\delta}$ materials to compare our predictions for CTO against.[30] The pristine material was reported to have a negligible $\sigma = 10^{-5}$ S cm^{-1} at 1000 K, but introducing O vacancies produced a much larger $n \approx 2 \times 10^{20}$ cm^{-3} and $\sigma \approx 100$ S cm^{-1} with $S = -375$ μV K^{-1}. With $n = 2.5 \times 10^{20}$, our calculations predict $\sigma = 36$ S cm^{-1} and $S = -331$ μV K^{-1}, which we again consider to be reasonable agreement. For a variety of La-doped samples, for which we estimate that $n > 10^{21}$ cm^{-3}, maximum σ and S around 250 S cm^{-1} and -175 μV K^{-1} were measured at 1000 K, and using $n = 10^{21}$ cm^{-3} we predict values of 144 S cm^{-1} and -215 μV K^{-1} respectively. Our predictions for CTO are generally closer to measurements than those for STO, which, given that we would expect the measurements on CTO to be on the orthorhombic phase modelled in the calculations,[65] supports the suggestion that some of the discrepancies in our predictions for STO can indeed be put down to the calculations being performed on the tetragonal rather than the cubic phase.

Qualitatively, all three sets of experiments indicate a decrease in σ and an increase in the absolute value of S with temperature, consistent with our predictions. Unfortunately, the majority of these papers do not separate the thermal conductivity into electronic and lattice contributions, but the measurements in ref. 30 suggest values of <1 W m^{-1} K^{-1} at 1000 K and n on the order of 10^{20} cm^{-3}, which is again consistent with our predictions.

3.4 Thermoelectric figure of merit

We now combine the calculated electrical-transport and κ_{latt} to predict the thermoelectric figure of merit ZT as a function of doping level and temperature using eqn (1) (Fig. 5). We summarise the minimal temperatures and n for which $ZT > 1$, and the corresponding transport properties, in Table 4, together with the predicted ZT_{max} at $T = 400$, 600 and 1000 K corresponding roughly to the low- mid- and high-temperature heat-recovery scenarios in ref. 86.

We predict that the industry-standard $ZT = 1$ can be achieved for STO at 1480 K with $n = 10^{21}$, and for CTO at 1640 K with $n = 5 \times 10^{20}$ cm^{-3}. On the other hand, we predict BTO can achieve a ZT_{max} of just 0.64 with $n = 2.5 \times 10^{21}$ cm^{-3} and at $T = 1800$ K.

At 1000 K, we predict ZT_{max} of 0.560 for CTO, 0.535 for STO, and 0.214 for BTO, all of which require n on the order of 10^{21} cm^{-3}. At lower temperatures of 400 and 600 K, we predict much smaller ZT_{max} of 0.07–0.22 at 600 K and 0.03–0.09 at 400 K, which also require similarly large n. While the combination of a higher Seebeck coefficient but lower electrical conductivity results in ~10–40% larger PFs at higher temperatures, the increase in ZT with temperature is largely dominated by a ~60% fall in the lattice thermal conductivity.

CTO and STO are predicted to have similar ZT due to a balance of a ~30–40% larger PF in STO and a ~30% smaller κ_{latt} in CTO. On the other hand, BTO is predicted to have a lower Seebeck coefficient, conductivity and power factor than the other two perovskites and a comparable κ_{latt} to CTO, resulting in lower ZT. This comparison suggests the ZT of CTO a could potentially be enhanced by improving the electrical properties, specifically the conductivity, and the ZT of STO could be improved by reducing the κ_{latt}.

Given the relatively small anisotropy in the predicted electrical properties and κ_{latt}, we predict that the ZT are relatively

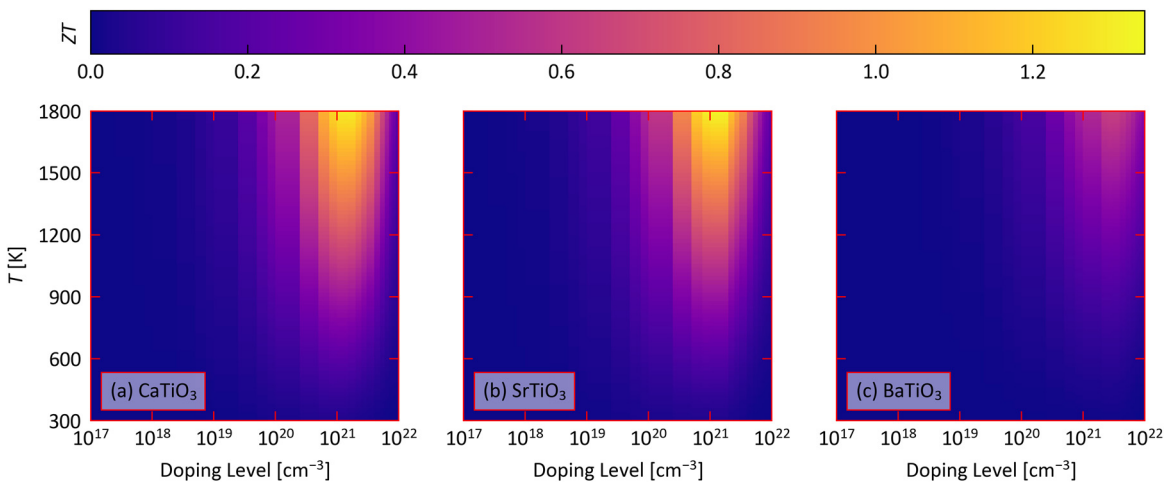

Fig. 5 Predicted thermoelectric figure of merit ZT of $CaTiO_3$ (a), $SrTiO_3$ (b) and $BaTiO_3$ (c) as a function of doping level n and temperature obtained using eqn (1).

Table 4 Predicted average ZT of $CaTiO_3$, $SrTiO_3$ and $BaTiO_3$, calculated using eqn (1), together with the associated temperature T, carrier concentration n, Seebeck coefficient S, electrical conductivity σ, power factor $S^2\sigma$ (PF), and lattice, electronic and total thermal conductivity κ_{latt}, κ_{el} and κ_{tot}. ZT values are given at four temperatures, *viz.* T = 400, 600 and 1000 K, corresponding roughly to the low-, medium- and high-temperatures outlined in ref. 86, and the minimum temperature at which we predict $ZT > 1$ can be obtained (for $BaTiO_3$ we show the temperature at which the largest ZT is obtained)

							κ [W m^{-1} K^{-1}]		
	T [K]	n [cm^{-3}]	ZT	S [μV K^{-1}]	σ [S cm^{-1}]	$S^2\sigma$ (PF) [mW m^{-1} K^{-2}]	κ^{el}	κ^{latt}	κ_{tot}
$CaTiO_3$	400	7.5×10^{20}	0.09	−150	265	0.60	0.21	2.40	2.61
	600	1×10^{21}	0.22	−168	240	0.68	0.27	1.60	1.87
	1000	1×10^{21}	0.56	−215	144	0.67	0.23	0.96	1.19
	1640	5×10^{20}	1	−312	41.6	0.41	0.08	0.65	0.73
$SrTiO_3$	400	7.5×10^{20}	0.08	−128	484	0.79	0.40	3.39	3.79
	600	7.5×10^{20}	0.21	−169	322	0.91	0.37	2.31	2.68
	1000	7.5×10^{20}	0.54	−219	193	0.93	0.33	1.40	1.73
	1480	7.5×10^{20}	1	−256	128	0.84	0.29	0.95	1.24
$BaTiO_3$	400	2.5×10^{21}	0.03	−93.6	265	0.23	0.24	3.31	3.54
	600	2.5×10^{21}	0.07	−124	185	0.29	0.23	2.19	2.42
	1000	2.5×10^{21}	0.21	−166	119	0.33	0.23	1.31	1.54
	1800	2.5×10^{21}	0.64	−218	70.3	0.33	0.21	0.73	0.93

isotropic (Fig. S16–S18, ESI†). In CTO, the ZT is largest along the a direction and smallest along the b direction, at ∼5–10% larger and 10–15% smaller than the average value, respectively, depending on the temperature. This is due to the anisotropy in the electrical conductivity and power factor. In STO, the ZT is 6–8% larger than the average along the equivalent a and b directions and ∼10–15% smaller along the c direction, due largely to the anisotropy in the lattice thermal conductivity. In BTO, on the other hand, the ZT varies by a more modest ∼1–5% and is largest along the equivalent a and b directions.

Despite the disagreement in some of the predicted electrical- and thermal-transport properties to experiments, comparison with the literature suggests the predicted ZT are very reasonable. Ref. 30 investigated 20% La-doped $CaTiO_3$ with $n \approx 2.0 \times 10^{20}$ cm^{-3} and obtained $ZT \approx 0.1$ at T = 300 K and 0.4 at T = 1100 K. With $n = 2.5 \times 10^{20}$ cm^{-3} and T = 300 K, we predict a smaller ZT = 0.04, while at the higher T = 1100 K we predict a similar ZT = 0.45. We ascribe the discrepancy at low temperature to the likely impact of the doping on reducing the κ_{latt}. Ref. 89 investigated 8% Pm-doped STO and obtained a ZT of 0.64 at 1200 K. While the authors do not quote a carrier concentration, we obtain and a similar ZT = 0.68 with $n = 5 \times 10^{20}$ cm^{-3}. We were unfortunately not able to find ZT values for n-type $BaTiO_3$ for comparison.

As noted above, comparison of the predicted electrical and thermal transport properties to experiments suggests a tendency for the calculations to overestimate the power factors and underestimate the lattice thermal conductivities. This should in principle lead to an overestimate of the ZT. The fact that the predicted ZT are close to the experimental values therefore suggests these discrepancies have a small impact on the calculated figure of merit, at least at the higher temperatures and n for which the largest ZT_{max} are obtained.

4 Conclusions

In this work we have applied a fully *ab initio* approach to model the electrical- and thermal-transport properties and thermoelectric figure of merit of orthorhombic $CaTiO_3$, tetragonal $SrTiO_3$, and rhombohedral $BaTiO_3$. The differences in the electrical properties are dominated by the electrical conductivity, and the piezoelectric scattering enabled by the non-centrosymmetric *R3m* spacegroup of BTO results in a significant suppression of the σ. We predict that doping levels on the order of 10^{21} cm^{-3} are required to obtain reasonable power factors, while larger n have a detrimental impact on the Seebeck coefficients. The lattice thermal conductivity plays an important role in determining the ZT, with a steep temperature dependence resulting in the benchmark $ZT > 1$ only being attained at high temperatures. Analysis of the κ_{latt} demonstrates that differences in structure and chemical bonding, rather than the mass of the A-site cation, is the key descriptor, and that the relatively high thermal conductivity of STO is due to large phonon group velocities.

The relatively good agreement between our calculations and experimental measurements, in particular for the predicted ZT, demonstrates considerable promise for the application of our workflow to other perovskites and oxides more generally. In particular, our calculations suggest it is possible to make a good estimate of the ZT_{max} and the carrier concentration and temperature required to achieve it, which could provide an indication of potential applications and whether the required doping level is feasible. These calculations could therefore serve as a valuable complement to experiments in the ongoing search for high-performance oxide thermoelectrics. However, for improved quantitative predictions it is likely to be necessary to investigate the impact of the crystal structure in more detail, and to establish the impact of dopants and vacancies present at high concentrations (few at%) on the electrical and thermal properties. We aim to explore both of these topics in future studies.

Author contributions

Conceptualisation – JMS; methodology – all authors; data curation – all authors; formal analysis and investigation – all

authors; writing (original draft) – AZK and JMF; writing (review and editing) – all authors; funding acquisition – JMS. All authors have read and agreed to the published version of the paper.

Data-access statement

Raw data from the calculations performed in this study will be made available to download free of charge from an online repository at **https://doi.org/10.17632/mzwcgry9dd**.

Conflicts of interest

There are no conflicts to declare.

Acknowledgements

We acknowledge helpful comments from Prof. Nikolas Kaltsoyannis at the University of Manchester (UoM) on a draft version of this manuscript. AZK is supported by a UoM PhD studentship. JMS and JMF are supported by a UKRI Future Leaders Fellowship (MR/T043121/1), and JMS previously held a UoM Presidential Fellowship. *Via* our membership of the UK's HEC Materials Chemistry Consortium, which is funded by EPSRC (EP/R029431 and EP/X035859), this work used the ARCHER2 UK National Supercomputing Service (**https://www.archer2.ac.uk**). A subset of our calculations also made use of the UoM Computational Shared Facility (CSF) computing cluster, which is maintained by UoM Research IT.

Notes and references

1 G. Tan, L.-D. Zhao and M. G. Kanatzidis, *Chem. Rev.*, 2016, **116**, 12123–12149.
2 H. Ritchie, M. Roser and P. Rosado, CO_2 and Greenhouse Gas Emissions, 2020, **https://ourworldindata.org/co2-and-greenhouse-gas-emissions**.
3 R. Freer and A. V. Powell, *J. Mater. Chem. C*, 2020, **8**, 441–463.
4 W. G. Zeier, A. Zevalkink, Z. M. Gibbs, G. Hautier, M. G. Kanatzidis and G. J. Snyder, *Angew. Chem., Int. Ed.*, 2016, **55**, 6826–6841.
5 C. Li, J. Hong, A. May, D. Bansal, S. Chi, T. Hong, G. Ehlers and O. Delaire, *Nat. Phys.*, 2015, **11**, 1063–1069.
6 U. Aseginolaza, R. Bianco, L. Monacelli, L. Paulatto, M. Calandra, F. Mauri, A. Bergara and I. Errea, *Phys. Rev. Lett.*, 2019, **122**, 075901.
7 U. Aseginolaza, R. Bianco, L. Monacelli, L. Paulatto, M. Calandra, F. Mauri, A. Bergara and I. Errea, *Phys. Rev. B*, 2019, **100**, 214307.
8 M. D. Nielsen, V. Ozolins and J. P. Heremans, *Energy Environ. Sci.*, 2013, **6**, 570–578.
9 K. Biswas, J. He, I. D. Blum, C.-I. Wu, T. P. Hogan, D. N. Seidman, V. P. Dravid and M. G. Kanatzidis, *Nature*, 2012, **489**, 414–418.
10 Z. M. Gibbs, H. Kim, H. Wang, R. L. White, F. Drymiotis, M. Kaviany and G. Jeffrey Snyder, *Appl. Phys. Lett.*, 2013, **103**, 262109.
11 O. Delaire, J. Ma, K. Marty, A. F. May, M. A. McGuire, M.-H. Du, D. J. Singh, A. Podlesnyak, G. Ehlers, M. D. Lumsden and B. C. Sales, *Nat. Mater.*, 2011, **10**, 614–619.
12 D. Champier, *Energy Convers. Manage.*, 2017, **140**, 167–181.
13 I. Terasaki, *Phys. Rev. B: Condens. Matter Mater. Phys.*, 1997, **56**, 685–687.
14 H. Yakabe, K. Kikuchi, I. Terasaki, Y. Sasago and K. Uchinokura, *Proceedings of the 1997 16th International Conference on Thermoelectrics*, 1997, pp. 523–527.
15 W. Koshibae, K. Tsutsui and S. Maekawa, *Phys. Rev. B: Condens. Matter Mater. Phys.*, 2000, **62**, 6869–6872.
16 Y. Miyazaki, *Solid State Ionics*, 2004, **172**, 463–467.
17 M. Shikano and R. Funahashi, *Appl. Phys. Lett.*, 2003, **82**, 1851–1853.
18 H. Fukutomi, Y. Konno, K. Okayasu, M. Hasegawa and H. Nakatsugawa, *Mater. Sci. Eng., A*, 2009, **527**, 61–64.
19 J. D. Baran, M. Molinari, N. Kulwongwit, F. Azough, R. Freer, D. Kepaptsoglou, Q. M. Ramasse and S. C. Parker, *J. Phys. Chem. C*, 2015, **119**, 21818–21827.
20 R. Funahashi, I. Matsubara and S. Sodeoka, *Appl. Phys. Lett.*, 2000, **76**, 2385–2387.
21 J. Diez, E. Guilmeau, M. Madre, S. Marinel, S. Lemonnier and A. Sotelo, *Solid State Ionics*, 2009, **180**, 827–830.
22 E. Combe, R. Funahashi, T. Barbier, F. Azough and R. Freer, *J. Mater. Res.*, 2016, **31**, 1296–1305.
23 T. Tsubota, M. Ohtaki, K. Eguchi and H. Arai, *J. Mater. Chem.*, 1997, **7**, 85–90.
24 T. Okuda, K. Nakanishi, S. Miyasaka and Y. Tokura, *Phys. Rev. B: Condens. Matter Mater. Phys.*, 2001, **63**, 113104.
25 H. Muta, K. Kurosaki and S. Yamanaka, *J. Alloys Compd.*, 2003, **350**, 292–295.
26 H. Muta, K. Kurosaki and S. Yamanaka, *J. Alloys Compd.*, 2005, **392**, 306–309.
27 T. Kobayashi, H. Takizawa, T. Endo, T. Sato, M. Shimada, H. Taguchi and M. Nagao, *J. Solid State Chem.*, 1991, **92**, 116–129.
28 D. Flahaut, T. Mihara, R. Funahashi, N. Nabeshima, K. Lee, H. Ohta and K. Koumoto, *J. Appl. Phys.*, 2006, **100**, 084911.
29 D. A. Muller, N. Nakagawa, A. Ohtomo, J. L. Grazul and H. Y. Hwang, *Nature*, 2004, **430**, 657–661.
30 J. Li, Y. Wang, X. Yang, H. Kang, Z. Cao, X. Jiang, Z. Chen, E. Guo and T. Wang, *Chem. Eng. J.*, 2022, **428**, 131121.
31 R. King-Smith and D. Vanderbilt, *Phys. Rev. B: Condens. Matter Mater. Phys.*, 1994, **49**, 5828–5844.
32 S. Dahbi, N. Tahiri, O. El Bounagui and H. Ez-Zahraouy, *Chem. Phys.*, 2021, **544**, 111105.
33 A. M. Ganose, J. Park, A. Faghaninia, R. Woods-Robinson, K. A. Persson and A. Jain, *Nat. Commun.*, 2021, **12**, 2222.
34 A. Togo, L. Chaput and I. Tanaka, *Phys. Rev. B: Condens. Matter Mater. Phys.*, 2015, **91**, 094306.
35 J. M. Flitcroft, I. Pallikara and J. M. Skelton, *Solids*, 2022, **3**, 155–176.
36 W. Rahim, J. M. Skelton and D. O. Scanlon, *J. Mater. Chem. A*, 2020, **8**, 16405–16420.

37 K. Brlec, K. B. Spooner, J. M. Skelton and D. O. Scanlon, *J. Mater. Chem. A*, 2022, **10**, 16813–16824.
38 K. Momma and F. Izumi, *J. Appl. Crystallogr.*, 2011, **44**, 1272–1276.
39 R. Ali and M. Yashima, *J. Solid State Chem.*, 2005, **178**, 2867–2872.
40 J. M. Kiat and T. Roisnel, *J. Phys.: Condens. Matter*, 1996, **8**, 3471.
41 A. W. Hewat, *Ferroelectrics*, 1973, **6**, 215–218.
42 G. Kresse and J. Hafner, *Phys. Rev. B: Condens. Matter Mater. Phys.*, 1993, **47**, 558–561.
43 A. Jain, S. P. Ong, G. Hautier, W. Chen, W. D. Richards, S. Dacek, S. Cholia, D. Gunter, D. Skinner, G. Ceder and K. A. Persson, *APL Mater.*, 2013, **1**, 011002.
44 J. P. Perdew, A. Ruzsinszky, G. I. Csonka, O. A. Vydrov, G. E. Scuseria, L. A. Constantin, X. Zhou and K. Burke, *Phys. Rev. Lett.*, 2008, **100**, 136406.
45 P. E. Blöchl, *Phys. Rev. B: Condens. Matter Mater. Phys.*, 1994, **50**, 17953–17979.
46 G. Kresse and D. Joubert, *Phys. Rev. B: Condens. Matter Mater. Phys.*, 1999, **59**, 1758–1775.
47 H. J. Monkhorst and J. D. Pack, *Phys. Rev. B: Condens. Matter Mater. Phys.*, 1976, **13**, 5188–5192.
48 A. Togo and I. Tanaka, *Scr. Mater.*, 2015, **108**, 1–5.
49 X. Gonze and C. Lee, *Phys. Rev. B: Condens. Matter Mater. Phys.*, 1997, **55**, 10355–10368.
50 M. Gajdoš, K. Hummer, G. Kresse, J. Furthmüller and F. Bechstedt, *Phys. Rev. B: Condens. Matter Mater. Phys.*, 2006, **73**, 045112.
51 A. V. Krukau, O. A. Vydrov, A. F. Izmaylov and G. E. Scuseria, *J. Chem. Phys.*, 2006, **125**, 224106.
52 J. M. Skelton, D. S. D. Gunn, S. Metz and S. C. Parker, *J. Chem. Theory Comput.*, 2020, **16**, 3543–3557.
53 J. P. Perdew, K. Burke and M. Ernzerhof, *Phys. Rev. Lett.*, 1996, **77**, 3865–3868.
54 D. Porezag and M. R. Pederson, *Phys. Rev. B: Condens. Matter Mater. Phys.*, 1996, **54**, 7830–7836.
55 J. M. Skelton, L. A. Burton, A. J. Jackson, F. Oba, S. C. Parker and A. Walsh, *Phys. Chem. Chem. Phys.*, 2017, **19**, 12452–12465.
56 A. M. Glazer, *Acta Crystallogr., Sect. B: Struct. Crystallogr. Cryst. Chem.*, 1972, **28**, 3384–3392.
57 M. Morana, J. Wiktor, M. Coduri, R. Chiara, C. Giacobbe, E. L. Bright, F. Ambrosio, F. De Angelis and L. Malavasi, *J. Phys. Chem. Lett.*, 2023, **14**, 2178–2186.
58 J. C. Slater, *J. Chem. Phys.*, 2004, **41**, 3199–3204.
59 Z. Zhang, K. Yuan, J. Zhu, X. Fan, J. Zhou and D. Tang, *Appl. Phys. Lett.*, 2022, **120**, 262201.
60 K. Parlinski, Z. Q. Li and Y. Kawazoe, *Phys. Rev. Lett.*, 1997, **78**, 4063–4066.
61 A. J. Ahmed, S. M. K. Nazrul Islam, R. Hossain, J. Kim, M. Kim, M. Billah, M. S. A. Hossain, Y. Yamauchi and X. Wang, *R. Soc. Open Sci.*, 2019, **6**, 190870.
62 S. P. Singh, N. Kanas, T. D. Desissa, M. Johnsson, M.-A. Einarsrud, T. Norby and K. Wiik, *J. Eur. Ceram. Soc.*, 2020, **40**, 401–407.
63 S. Ohta, T. Nomura, H. Ohta and K. Koumoto, *J. Appl. Phys.*, 2005, **97**, 034106.
64 R. He, H. Wu, L. Zhang, X. Wang, F. Fu, S. Liu and Z. Zhong, *Phys. Rev. B*, 2022, **105**, 064104.
65 F. Guyot, P. Richet, P. Courtial and P. Gillet, *Phys. Chem. Miner.*, 1993, **20**, 141–146.
66 H. J. Goldsmid, *Proc. Phys. Soc., London, Sect. B*, 1956, **69**, 203.
67 I. T. Witting, T. C. Chasapis, F. Ricci, M. Peters, N. A. Heinz, G. Hautier and G. J. Snyder, *Adv. Electron. Mater.*, 2019, **5**, 1800904.
68 P.-C. Wei, S. Bhattacharya, J. He, S. Neeleshwar, R. Podila, Y. Y. Chen and A. M. Rao, *Nature*, 2016, **539**, E1–E2.
69 R. Banerjee, S. Chatterjee, M. Ranjan, T. Bhattacharya, S. Mukherjee, S. S. Jana, A. Dwivedi and T. Maiti, *ACS Sustainable Chem. Eng.*, 2020, **8**, 17022–17032.
70 L.-D. Zhao, S.-H. Lo, Y. Zhang, H. Sun, G. Tan, C. Uher, C. Wolverton, V. P. Dravid and M. G. Kanatzidis, *Nature*, 2014, **508**, 373–377.
71 J. Tang and J. M. Skelton, *J. Phys.: Condens. Matter*, 2021, **33**, 164002.
72 J. M. Skelton, *J. Mater. Chem. C*, 2021, **9**, 11772–11787.
73 B. Wei, J. M. Flitcroft and J. M. Skelton, *Molecules*, 2022, **27**, 6431.
74 J. Cen, I. Pallikara and J. M. Skelton, *Chem. Mater.*, 2021, **33**, 8404–8417.
75 A. Krause, W. M. Weber, D. Pohl, B. Rellinghaus, A. Kersch and T. Mikolajick, *J. Phys. D: Appl. Phys.*, 2015, **48**, 415304.
76 M. C. Oliveira, R. A. P. Ribeiro, E. Longo, M. R. D. Bomio, F. V. Motta and S. R. de Lazaro, *Int. J. Quantum Chem.*, 2020, **120**, e26054.
77 R. A. Evarestov and A. V. Bandura, *J. Comput. Chem.*, 2012, **33**, 1123–1130.
78 C. Adamo and V. Barone, *J. Chem. Phys.*, 1999, **110**, 6158–6170.
79 M. Kar, *Electronic and optical properties of $SrTiO_3$* perovskite using semi-local and hybrid first principles density functional theory*, 2021.*
80 M. Cardona, *Phys. Rev.*, 1965, **140**, A651–A655.
81 M.-S. Lee and S. D. Mahanti, *Phys. Rev. B: Condens. Matter Mater. Phys.*, 2012, **85**, 165149.
82 X.-L. Shi, H. Wu, Q. Liu, W. Zhou, S. Lu, Z. Shao, M. Dargusch and Z.-G. Chen, *Nano Energy*, 2020, **78** 105195.
83 J. Ravichandran, W. Siemons, D.-W. Oh, J. T. Kardel, A. Chari, H. Heijmerikx, M. L. Scullin, A. Majumdar, R. Ramesh and D. G. Cahill, *Phys. Rev. B: Condens. Matter Mater. Phys.*, 2010, **82**, 165126.
84 J. Wang, B.-Y. Zhang, H.-J. Kang, Y. Li, X. Yaer, J.-F. Li, Q. Tan, S. Zhang, G.-H. Fan, C.-Y. Liu, L. Miao, D. Nan, T.-M. Wang and L.-D. Zhao, *Nano Energy*, 2017, **35**, 387–395.
85 S. Ohta, T. Nomura, H. Ohta, M. Hirano, H. Hosono and K. Koumoto, *Appl. Phys. Lett.*, 2005, **87**, 092108.
86 S. LeBlanc, S. K. Yee, M. L. Scullin, C. Dames and K. E. Goodson, *Renewable Sustainable Energy Rev.*, 2014, **32**, 313–327.

87 A. Chatterjee, Z. Lan, D. V. Christensen, F. Bauitti, A. Morata, E. Chavez-Angel, S. Sanna, I. E. Castelli, Y. Chen, A. Tarancon and N. Pryds, *Phys. Chem. Chem. Phys.*, 2022, **24**, 3741–3748.
88 D. Narducci, E. Selezneva, G. Cerofolini, S. Frabboni and G. Ottaviani, *J. Solid State Chem.*, 2012, **193**, 19–25.
89 A. A. Adewale, A. Chik, R. M. Zaki, F. C. Pa, Y. C. Keat and N. H. Jamil, *Sustainable Mater.*, 2018, 3–8.